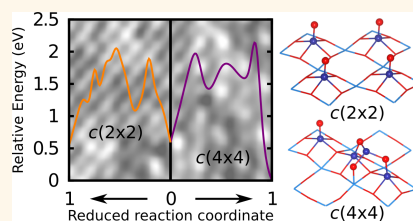# Coexisting Surface Phases and Coherent One-Dimensional Interfaces on BaTiO$_3$(001)

Erie H. Morales,[†,⊥,*] John Mark P. Martirez,[‡,⊥] Wissam A. Saidi,[§] Andrew M. Rappe,[‡] and Dawn A. Bonnell[†]

[†]Department of Materials Science and Engineering, University of Pennsylvania, Philadelphia, Pennsylvania 19104−6202, United States, [‡]The Makineni Theoretical Laboratories, Department of Chemistry, University of Pennsylvania, Philadelphia, Pennsylvania 19104−6323, United States, and [§]Department of Chemical and Petroleum Engineering, University of Pittsburgh, Pittsburgh, Pennsylvania 15261, United States. [⊥]E.H.M. and J.M.P.M. contributed equally.

ABSTRACT Coexistence of surface reconstructions is important due to the diversity in kinetic and thermodynamic processes involved. We identify the coexistence of kinetically accessible phases that are chemically identical and form coherent interfaces. Here, we establish the coexistence of two phases, $c(2 \times 2)$ and $c(4 \times 4)$, in BaTiO$_3$(001) with atomically resolved Scanning Tunneling Microscopy (STM). First-principles thermodynamic calculations determine that TiO adunits and clusters compose the surfaces. We show that TiO diffusion results in a kinetically accessible $c(2 \times 2)$ phase, while TiO clustering results in a kinetically and thermodynamically stable $c(4 \times 4)$ phase. We explain the formation of domains based on the diffusion of TiO units. The diffusion direction determines the observed 1D coherent interfaces between $c(2 \times 2)$ and $c(4 \times 4)$ reconstructions. We propose atomic models for the $c(2 \times 2)$, $c(4 \times 4)$, and 1D interfaces.

There is renewed interest in BaTiO$_3$ and related oxides due to recent demonstrations of their versatile surface properties. *In situ* ferroelectric poling has been shown to control surface reactions,[1] as well as the converse effect in which adsorbates control the polarization.[2−4] Complex metal oxide surfaces are interesting both from a fundamental perspective and for the promise they hold for practical applications. Compelling interest stems from the ability of transition metal cations to induce structural complexity and functional properties.[5−22] Nevertheless, this family of materials represents an experimental and theoretical challenge. In perovskites the coexistence of different surface structures has been shown using STM,[5−12] but the origin of such coexistence has not been mechanistically considered. In this study, we use electronic structure measurements in tandem with first-principles density functional theory (DFT) to obtain the most precise atomistic model of the coexisting phases that we experimentally observe on BaTiO$_3$. Additionally, we elucidate the atomic and electronic structures of two phases, the $c(2 \times 2)$ and $c(4 \times 4)$ reconstructions of BaTiO$_3$. We conclude that TiO and TiO-clusters allow the kinetic coexistence of the two reconstructions. We show that the $c(2 \times 2)$ surface is a trapped kinetic phase while the $c(4 \times 4)$ is the equilibrium thermodynamic phase, and explain their domain formation. Furthermore, we observe that at the meeting of these phases 1D coherent interfaces form. We precisely address the atomic details of the 1D coherent interfaces between the phases.

Depending on thermochemical processing, BaTiO$_3$ develops a range of surface reconstructions: (1×1), (2×1), $c(2 \times 2)$, (3×2), (6×1),[23] (3×1), $(\sqrt{5} \times \sqrt{5})R26.6°$, and $(\sqrt{13} \times \sqrt{13})R33.6°$.[24−26] Each surface must be carefully considered in order to successfully model its composition. Here, determining the correct atomic structure involves the interplay of experimental and theoretical results where we employ the following four criteria: (1) DFT, from first-principles thermodynamics, we calculate the surface compositions with low free energy; (2) STM images, we compare STM simulations with experiment to find matching contrast variations; (3) electronic structure, from projected density of states (PDOS), we identify electronic spectral features of candidate structures; (4) Ti:O ratio, our previous

studies[24,26] provide an upper limit for the expected reduction of the structures in consideration.

The above-mentioned criteria were employed to evaluate the structure of the smaller reconstruction ($c(2 \times 2)$), where the reasonable simulation size enabled us to explore a wide range in the chemical phase space (various compositions) in our DFT calculations. On the basis of chemical constraints, the established $c(2 \times 2)$ composition will point to the potential candidates for the coexisting $c(4 \times 4)$ phase as we illustrate below. This allowed us to limit the variations in the chemical composition of the $c(4 \times 4)$ structures, and we concentrated instead on structural permutations. To solve for the $c(4 \times 4)$ structure, we rely on points (1−3) as discussed above. In the present study, we elucidate the atomic and electronic structures of two phases, the $c(2 \times 2)$ and $c(4 \times 4)$ reconstructions of $BaTiO_3$, and measure and calculate that they can coexist. We determine the thermodynamic and kinetic factors that lead to this stabilization and precisely address the atomic details of coherent interfaces between the phases.

RESULTS AND DISCUSSION

Surface Atomic Structures. Using DFT, we explore six structures of $BaTiO_3(001)$ surfaces exhibiting $c(2 \times 2)$ superstructures. These were selected in light of the results of past calculations involving a thorough investigation of the $(\sqrt{5} \times \sqrt{5})R26.6°$ reconstruction under reducing conditions.[26] We previously demonstrated that Ti-rich derivatives of the TiO_2 (001) surface have low surface free energies and produce electronic structure profiles consistent with experiment, whereas O vacancy or adatomic Ba models do not.

The experimental STM images of coexisting $c(2 \times 2)$ and $c(4 \times 4)$ phases are presented in Figure 1a,b. Both phases are in registry with the substrate, with bright features that have periodicities of 0.57 and 1.16 nm for the $c(2 \times 2)$ and $c(4 \times 4)$, respectively. The $c(2 \times 2)$ atomic structures are the result of either the formation of a TiO_x overlayer [TiO_2-TiO_2 and $TiO_2-TiO_{3/2}$] or the addition of TiO units [$TiO_2-(TiO)_{1/2}$], Ti adatoms [$TiO_2-Ti_{1/2}$], or both [$TiO_2-Ti_{1/2}(TiO)_{1/2}$], on a bulk-like TiO_2 surface. These structures are described in section II Supporting Information, Figure S1A, while the corresponding calculated STM images are shown in Figure S2. From comparison to the simulated STM images alone, the $c(2 \times 2)$ TiO_2-TiO_2 surface can be disregarded since the spatial contrast variations are not consistent with the experiment. Though the calculations of the structurally related double-layer reconstruction $TiO_2-TiO_{3/2}$ is similar to the experimental STM images, this composition is predicted to have a high surface energy within the experimental oxygen chemical potential range, μ_O [−2.63, −3.88 eV], see section II Supporting Information, Figure S1B.

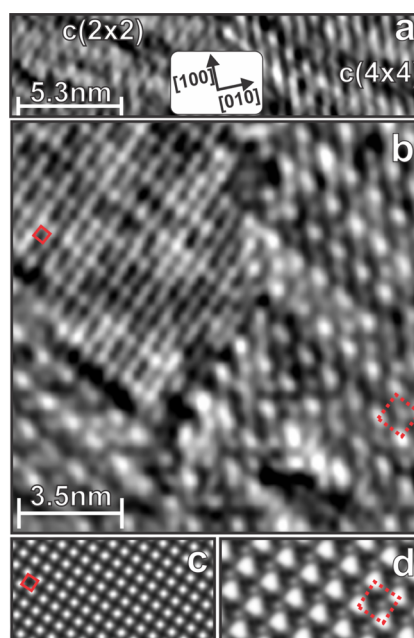**Figure 1.** Experimental and simulated STM images of the $c(2 \times 2)$ and $c(4 \times 4)$ surface reconstructions on $BaTiO_3(001)$. The experimental STM parameters are (a) (0.929 V, 0.15 nA) and (b) (1.008 V, 0.18 nA). Inset in (a) indicates crystallographic directions, that also apply to (b−d). Upper left portion shows $c(2 \times 2)$, while the rest shows $c(4 \times 4)$. DFT simulated STM for (c) $c(2 \times 2)$, and (d) $c(4 \times 4)$. Red squares indicate supercells of the reconstructions.

To determine the atomic structure of the reconstructions, we measure the local density of states (LDOS) to obtain electronic signatures that indicate the extent of the surface reduction. Calculations of atomic projected density of states (PDOS) for the surface Ti, Ti of the underlying bulk-like TiO_2 layer, and O adatoms provide further comparison with experiment. The LDOS of the reconstructions are presented in Figure 2a,b. The measured LDOS for both reconstructions have identical band gaps of 0.25 eV, with broad peaks associated with surface states below the Fermi level (0 V). These states are attributed to the occupied 3d states of reduced Ti species on the surface, narrowing the gap from 3.2 eV.[27,28] Aside from the clear indication of surface reduction, the similarity of the two surface electronic structures suggests a similar or identical chemical composition. From the simulated PDOS (Supporting Information, Figure S3), one can point out that excess Ti on the surface (i.e., higher Ti:O ratios) results in occupied Ti 3d-orbital derived states close to the valence band edge. Additionally, O adsorbates give rise to O 2p states that are higher in energy than the bulk O 2p states comprising the valence band. Incidentally, the lack of occupied Ti 3d orbitals in the TiO_2-TiO_2 and $TiO_2-TiO_{3/2}$ supports our previous conclusion, in which we discarded these as candidate structures. Thus, these fully oxidized or lightly reduced surfaces cannot account for the significant density of states near the Fermi level observed in the experiment.

The temperature at which the crystal is treated (1100 K) to form $c(2 \times 2)$ and $c(4 \times 4)$ is less than that used for the $(\sqrt{5} \times \sqrt{5})R26.6°$ reconstruction
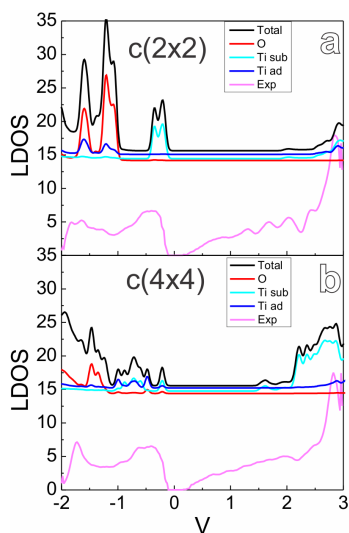

Figure 2. Experimental and calculated surface electronic structures. The measured LDOS spectra show narrowed surface band gaps and states near and below the Fermi level for both (a) $c(2 \times 2)$ and (b) $c(4 \times 4)$. These states indicate that the reconstructions are reduced, and DFT PDOS shows that they are due to occupied 3d orbitals of both subsurface and surface Ti, as well as O 2p orbitals of the O adatoms.

(1300 K).[24−26] This indicates a less reduced surface in the present case. We can define the surface Ti:O ratio from the Ti and O content of the reconstruction and the underlying bulk-like layer. Ti:O relates directly to the degree of surface reduction. More precisely, we determined the $(\sqrt{5} \times \sqrt{5})R26.6°$ to be $TiO_2-Ti_{3/5}$, with Ti content of $1 + 3/5 = 8/5$, and O content of 2, giving a Ti:O ratio of 4:5. Thus, 4:5 defines the upper limit ratio of the reconstructions found below 1300 K. The Ti:O ratios for the candidates vary from fully oxidized 1:2 [bulk-like TiO_2, TiO_2-TiO_2], to moderately reduced 4:7 [$TiO_2-TiO_{3/2}$] and 3:5 [$TiO_2-(TiO)_{1/2}$], to highly reduced 3:4 [$TiO_2-Ti_{1/2}$] and 4:5 [$TiO_2-Ti_{1/2}(TiO)_{1/2}$]. In consequence, we disregard the [$TiO_2-Ti_{1/2}(TiO)_{1/2}$] which has a 4:5 Ti:O ratio, inconsistent with the Ti:O progression, $c(2 \times 2) < \sqrt{5} \times \sqrt{5}R26.6°$ (4:5).[26]

The clustering behavior of the defects, as demonstrated by the $c(4 \times 4)$, requires a defect unit that is energetically favorable to aggregate. TiO units demonstrate such capability, in contrast to Ti adatoms as further discussed below. Therefore, a Ti adatom model ($TiO_2-Ti_{1/2}$) is less well able to explain the $c(4 \times 4)$ surface than a TiO adunit model, and its coexistence with $c(2 \times 2)$ strongly implies a similar extent of oxidation for both reconstructions. The factors described above lead to the proposed $c(2 \times 2)$ model, see Figure 3b, with a surface stoichiometry of $TiO_2-(TiO)_{1/2}$, a TiO_2 surface with half TiO coverage. Although
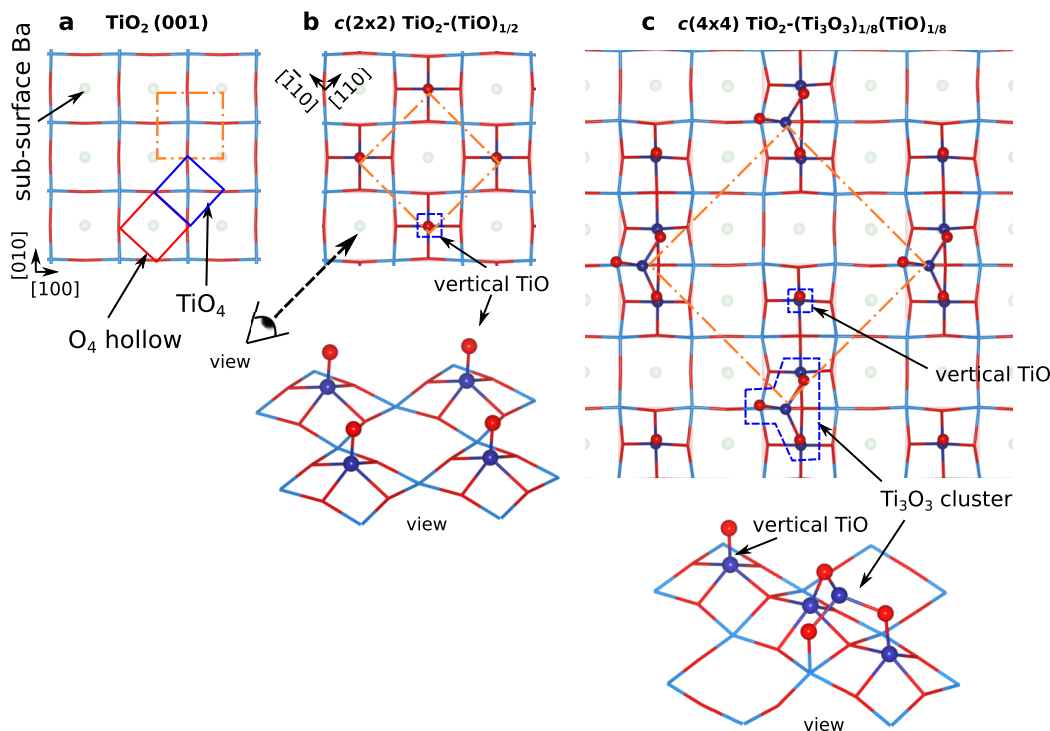

Figure 3. Calculated atomic structures of the BaTiO₃ reconstructions. Ball and stick models for the (a) bulk-like TiO_2 termination, (b) $c(2 \times 2)$, and (c) $c(4 \times 4)$ surfaces. The reconstructions exhibit TiO units adsorbed on a bulk-like TiO_2 surface. The TiO units are either isolated or in a cluster. Dark blue and red balls represent Ti and O adatoms, respectively. The dash-dotted lines mark the (a) 1×1, (b) $\sqrt{2} \times \sqrt{2}$, and (c) $2\sqrt{2} \times 2\sqrt{2}$ surface supercell. Angled views for both (b) and (c) are provided in the same viewing direction as shown in (b).

the TiO adunit model has two structural variations, the calculated surface energies favor one (structure discussed here) over the other, see section II of the Supporting Information. Figure 3a shows the bulk-like (001) TiO_2 termination which serves as the underlying structure ("subsurface") of the reconstruction. This subsurface layer is composed of corner shared TiO_4 units with O_4 hollow sites. The $c(2 \times 2)$ reconstruction is composed of vertically oriented TiO units, where each Ti is coordinated to four O atoms in the subsurface (O_4 hollow as defined in Figure 3a). The TiO units have nearest neighbors along [110] and [1$\bar{1}$0]. These TiO units are observed as bright contrast in the simulated STM $c(2 \times 2)$ image in Figure 1c. We propose that in the experimental STM $c(2 \times 2)$ image the bright features correspond to TiO units, upper left in Figure 1b. The surface LDOS spectrum shown in Figure 2a exhibits occupied Ti 3d-orbital derived states associated with the subsurface Ti (light blue) and Ti adatoms (dark blue). The high energy O 2p peaks (red) between -2.0 and -1.0 eV can be ascribed to π bonding orbitals between the Ti and O adatoms in the vertical TiO units. High covalency in these bonds is indicated by the overlapping Ti 3d and O 2p projections in this energy range. The match between the simulation and measurement strongly supports this assignment of the $c(2 \times 2)$ atomic structure.

From the similarity between the LDOS of the two reconstructions and their coexistence, we conclude that the $c(4 \times 4)$ is a derivative of $c(2 \times 2)$ resulting from some degree of agglomeration. The TiO units and Ti adatoms are positively charged defects that have partially donated their electrons to the subsurface Ti atoms *via* their bonds with the subsurface O atoms. Strong Coulombic repulsion between ions of the same charge discourages clustering of Ti^{n+} defects. However, surface O atoms, as in the TiO units, provide an avenue for agglomeration, as they mediate interactions between these Ti^{n+} ions while simultaneously satisfying their divalent nature by forming more bonds. A variety of structures with different TiO unit orderings and a net stoichiometry of TiO_2-$(TiO)_{1/2}$ which lead to $c(4 \times 4)$ periodicity have been explored, see section III of the Supporting Information and Figure S4. Among these structures, the surface $TiO_2-(Ti_3O_3)_{1/8}(TiO)_{1/8}$, whose structure is shown in Figure 3c, exhibits the lowest surface energy, and its simulated STM images is the most consistent with experiment (Figure 1d). The $c(4 \times 4)$ is composed of Ti_3O_3 clusters and isolated vertically oriented TiO units. The Ti_3O_3 cluster is formed by two vertical and one horizontal TiO units, arranged such that the cluster top has a TiO_3 subunit in a trigonal pyramidal geometry, and two Ti adatoms and one subsurface Ti support the three O adatoms, Figure 3c. It should be noted that the atomic features in the $c(4 \times 4)$ surface are larger and brighter than those of the $c(2 \times 2)$, and that the $c(4 \times 4)$ contains an additional

fainter off-center feature. The off-center vertical TiO unit and the Ti_3O_3 cluster are observed with bright contrast in the simulated STM image in Figure 1d, and the Ti_3O_3 is the brighter of the two (compare with experimental STM image in Figure 1b). The electronic spectrum of the $c(4 \times 4)$ structure, Figure 2b, exhibits similar occupied Ti 3d gap states as in $c(2 \times 2)$, however, with less overlap with the O adsorbate 2p states, indicative of reduced TiO bond covalency due to clustering.

Despite having similar electronic structure and the same composition in the two phases, the TiO unit and TiO clustering introduce significant chemical differences. The Ti atoms in the vertically oriented TiO units, as in the $c(2 \times 2)$ structure, are relatively inaccessible. Further, the O adatoms are unsaturated, subject to electrophilic attack to adopt a preferred 2-fold coordination. The clustering of the TiO units into Ti_3O_3, as in the $c(4 \times 4)$ structure, results in an exposed 3-fold coordinated Ti that is ready for nucleophilic attack (reduced Ti species are oxophilic.) Conversely, the O adatoms in the cluster are less susceptible to reaction, having satisfied 2-fold coordination. Considering the chemical similarities and differences presented above, it is necessary to address the mechanisms that lead to the coexistence of the $c(2 \times 2)$ and $c(4 \times 4)$ reconstructions.

Coexistence of the Two Phases. Since both $c(2 \times 2)$ and $c(4 \times 4)$ reconstructions have the same TiO coverage, there is no chemical driving force for interconversion. The relative energies are, therefore, a function of the Helmholtz free energy content associated with surface bond vibrations, see section IV of the Supporting Information. In Figure 4a we show the temperature dependent relative surface energy of the two reconstructions. The $c(4 \times 4)$ is approximately 0.16 eV/(1×1) surface cell, which is 0.32 eV/TiO, lower in energy than the $c(2 \times 2)$ across all temperatures. The vibrational contribution to the Helmholtz free energy provides insight into surface stability. Vibrational density of states indicates that the $c(4 \times 4)$ has a broader energy distribution in the low energy regime than does the $c(2 \times 2)$, see Figure 4b,c. Consequently, the $c(4 \times 4)$ has a more negative Helmholtz free energy of vibration. The $c(4 \times 4)$ is more stable than $c(2 \times 2)$ due to clustering that results in the valency increase of the O adatoms and softening of the surface vibrational modes. These considerations indicate that thermodynamic principles alone do not explain the experimentally observed coexistence of the $c(2 \times 2)$ and $c(4 \times 4)$ reconstructions, thus pointing to the role of kinetic considerations.

The formation of these reconstructions can be viewed as a gradual increase of TiO at the surface, with TiO units diffusing until an optimum concentration is reached. Figure 5a shows the coverage cascade, from bare TiO_2 surface to the optimum 4 TiO units per 8 unit
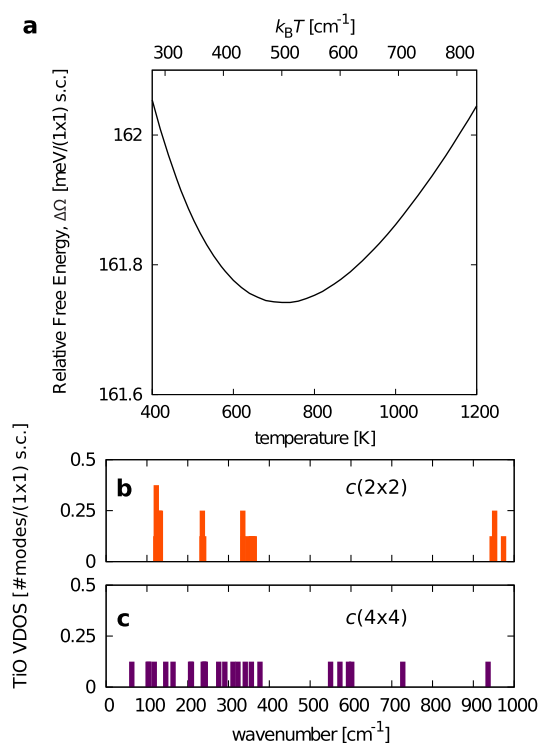
a

Figure 4. Surfaces' relative free energy and adatomic vibrational DOS. (a) Surface free energy of $c(2 \times 2)$ TiO$_2$–(TiO)$_{1/2}$ vs $c(4 \times 4)$ TiO$_2$–(Ti$_3$O$_3$)$_{1/8}$(TiO)$_{1/8}$ ($\Delta\Omega$ in energy per (1×1) surface cell, black curve) as a function of temperature. Also shown in the upper axis is thermal energy ($k_B T$) in wavenumbers. Surface TiO units' vibrational DOS (number of modes per (1×1) surface cell) for (b) $c(2 \times 2)$ TiO$_2$–(TiO)$_{1/2}$ (simulation size $2\sqrt{2} \times 2\sqrt{2}$) and (c) $c(4 \times 4)$ TiO$_2$–(Ti$_3$O$_3$)$_{1/8}$(TiO)$_{1/8}$.

cells coverage (in a $2\sqrt{2} \times 2\sqrt{2}$ surface super cell) with energies measured relative to the lowest energy structure in each tier. The propensity of the surface to transform into either one of the two reconstructions depends on the accessibility of the paths leading to them. Specifically, it depends on the relative rates for TiO to diffuse away from each other (favoring the $c(2 \times 2)$ structure) or to form small clusters (favoring the $c(4 \times 4)$ structure). The mere addition of TiO on the surface, without a preconceived notion of defect diffusion, would not exclusively form the $c(2 \times 2)$ TiO$_2$-(TiO)$_{1/2}$ and $c(4 \times 4)$ TiO$_2$-(Ti$_3$O$_3$)$_{1/8}$(TiO)$_{1/8}$, indicated with horizontally hatched and vertically hatched arrows in Figure 5a, respectively. It is interesting to note that the transitional structure (thick solid arrow, in Figure 5a) satisfies the following: (1) it is a precursor of both $c(2 \times 2)$ and $c(4 \times 4)$, (2) it is on the minimum-energy pathway from one reconstruction to the other, (3) it is energetically downhill for this phase to transform into either of the other phases, and (4) the two transformation paths are mutually exclusive. Figure 5b shows the calculated energy barriers of the transformation paths of the transitional phase into the $c(2 \times 2)$ and the $c(4 \times 4)$ (more details in section VI of the Supporting Information).

To explain the coexistence of the two, we can analyze the forward and reverse transformation paths

in Figure 5b. (a) The forward path starts at the center; the barrier heights of the two paths that lead to the $c(2 \times 2)$ vs $c(4 \times 4)$ are almost equal, 1.29 vs 1.36 eV/migrating TiO unit. This illustrates that at this surface coverage, dispersion and clustering have almost equivalent kinetic probabilities. (b) The reverse path starts at the end; the barrier heights from the $c(2 \times 2)$ vs $c(4 \times 4)$ are different, 1.18 vs 2.10 eV/migrating TiO. This illustrates that the $c(2 \times 2)$ is more likely to reverse its path back to the center. The TiO units are mobile at high temperatures, and free to diffuse and reorganize until three TiO units form a cluster, at which point breaking free from the cluster is both thermodynamically discouraged and kinetically improbable. Thus, while a $c(2 \times 2)$ can transform with relative ease, the $c(4 \times 4)$ clusters are very stable, thus terminating the process.

Domains and 1D interfaces. The coexistence of $c(2 \times 2)$ and $c(4 \times 4)$ implies the presence of interfaces between them. The experimental STM images reveal two distinct interfaces that run along the $[\bar{1}10]$ (left side) and the $[110]$ (right side) directions, shown in Figures 1b and 6a, upper panel. The $[\bar{1}10]$ interface can be characterized as a dark trench that is ≈ 1.1 nm ($2\sqrt{2}$ times the primitive cell) wide. The $[110]$ interface on the other hand is atomically sharp and narrower. In both cases, the reconstructions on either side of the interfaces have the bright spots of the $c(4 \times 4)$ aligned with every other row of the smaller spots of the $c(2 \times 2)$. Furthermore, the bright spots border the edge of the $c(4 \times 4)$.

The lack of 4-fold symmetry in the $c(4 \times 4)$ reconstruction helps us to determine the relative positions of the reconstructions and define probable candidate structures of the interfaces. The faint off-center STM image feature in the $c(4 \times 4)$ is toward the $[1\bar{1}0]$ direction, and therefore, this surface could only be oriented as is shown in Figure 3c. The structures shown in Figure 6b,c result in the best agreement between the simulated and experimental STM contrast for the $[\bar{1}10]$ and $[110]$ interfaces, respectively. See section V of the Supporting Information for other structures explored. The lower panels of Figure 6a show the composite calculated STM images of the interfaces and the two reconstructions. The dark trench in the $[\bar{1}10]$ interface (Figure 6a, lower left) is due to the absence of a TiO unit in the region that is 1.1 nm wide, indicated in Figure 6b. As a result, this interface has locally lower TiO coverage than the parent reconstructions. The $[110]$ interface (Figure 6a, lower right) is characterized as having a row of Ti$_3$O$_3$ clusters that is adjacent to a row of TiO. The proximity of the clusters to the TiO units induces a conformational change on every other TiO. The structure shows two types of geometries for the TiO units on the edge of $c(2 \times 2)$: the typical vertical orientation and a tilted geometry. The tilted geometry is a consequence of the repulsion between the O adatom
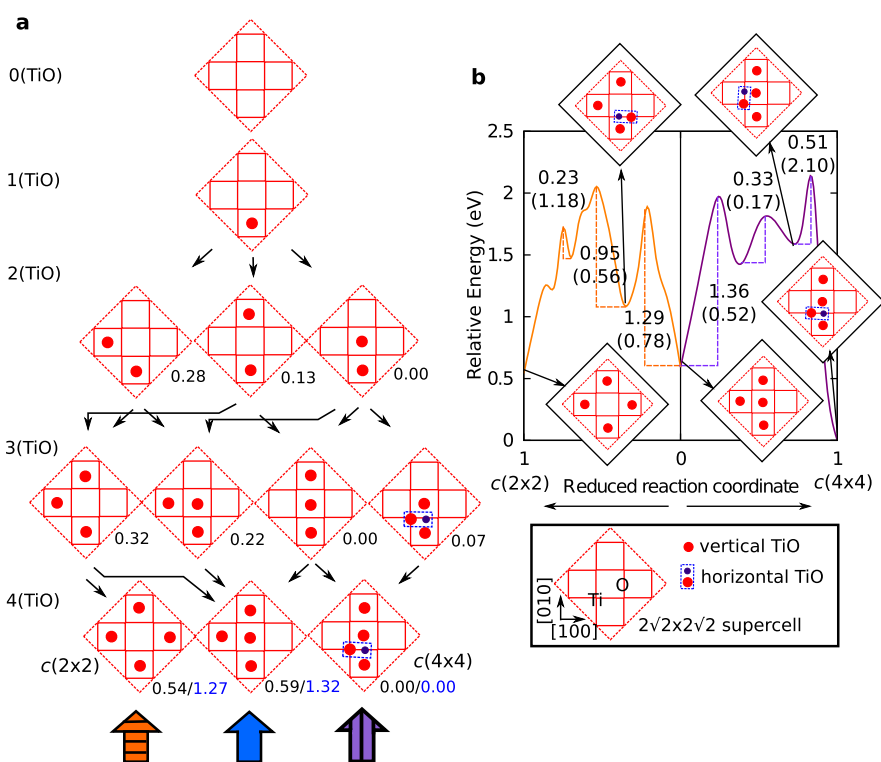
Figure 5. Surface transformation diagram and kinetics. (a) Starting from a clean TiO_2 surface, progressive addition of a TiO unit on the surface leads to different reconstructions, leading to the proposed $c(2 \times 2)$ and $c(4 \times 4)$ reconstructions with half monolayer TiO coverages. Energies from GGA (black) and/or GGA + U (blue), in eV/$2\sqrt{2} \times 2\sqrt{2}$ surface cell are given relative to the lowest energy structure of each tier. (b) Predicted GGA reaction barriers for the transformation of a transitional structure (0 reaction coordinate) to $c(2 \times 2)$, path toward left, and $c(4 \times 4)$, toward right. The energy barriers are shown for each pathway, where the numbers in parentheses are the barriers for the reverse of the paths. The thick arrows in (a) mark the kinetically relevant structures as described in the text.
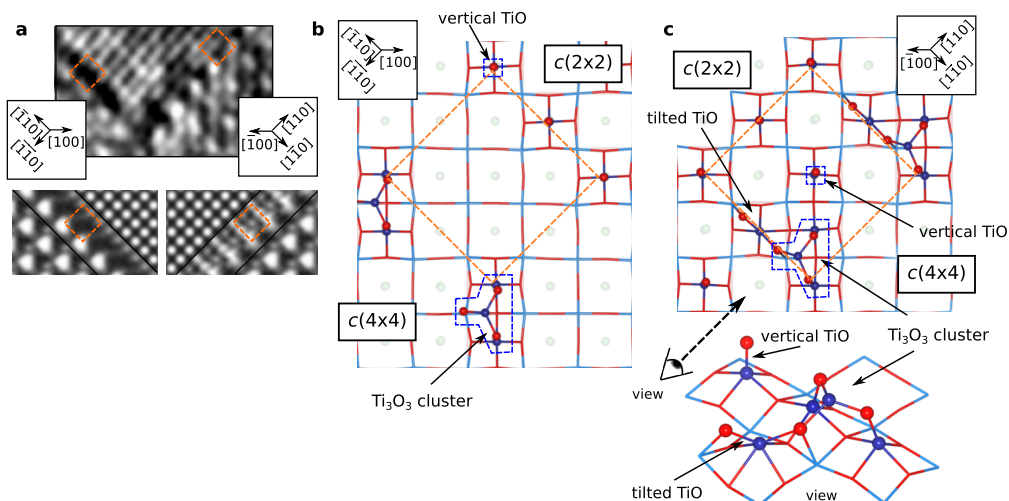

Figure 6. Proposed interfacial structures and their simulated STM images. (a) Experimental STM image showing two distinct interfaces between the $c(2 \times 2)$ and $c(4 \times 4)$ that run along [$\bar{1}$10] and [110] directions. Lower panel shows the composite of the simulated STM images for the reconstructions and the interfaces between them. Predicted atomic structures of the interfaces that run along (b) [$\bar{1}$10] and (c) [110]. Regions marked by dashed squares in the STM and structural models correspond to each other. An angled view is shown for structure (c), which emphasizes the Ti_3O_3 cluster closely adjacent to a TiO unit at the interface (compare with Figure 3c).

adsorbed on a subsurface Ti, belonging to the cluster, and the O adatom of the now tilted TiO. The interfaces are believed to be the result of the meeting of the growth edges of the domains of the $c(2 \times 2)$ and $c(4 \times 4)$ reconstructions. The prevalence of both the [$\bar{1}$10] and [110] interfaces, therefore, indicates preference for 45° growth edges in both reconstructions.

The preference for a 45° growth edge is closely related to the manner in which TiO migrates on the surface. The barrier for diffusion of a TiO unit unaided by a neighboring TiO unit is prohibitively large, 2.5 eV (see section VI of the Supporting Information). Thus, TiO has a limited diffusion length of only one unit cell to remain adjacent to another TiO. However, the diffusion length along [110] (diagonal diffusion) could be extended by a row of TiO adunits along this direction, thus effectively creating growth edges along the lattice diagonal. The mechanism of diagonal *vs* horizontal/vertical ([100]/[010]) diffusion is illustrated in section VII of the Supporting Information. The growth of domains is schematically shown in Figure 7. Domain growth is achieved through the extension of the TiO chain along [110] or [$\bar{1}$10] for both reconstructions. Growth is achieved by a combination of two types of TiO diffusion: (1) toward the edge, and (2) at the edge. (1) TiO is delivered near the edge *via* the low barrier diagonal diffusion (green circles with diagonal arrows). (2) The domain is extended by one unit cell through horizontal or vertical diffusion at the growth edge (green circles with horizontal/vertical arrows). The growth of the $c(4 \times 4)$ and $c(2 \times 2)$ domains is shown at different stages of completion in boxes 1−4 and boxes 5−7, respectively, see Figure 7. The transitional structures form boxes 1−3 and boxes 5 and 6 that transform into either $c(4 \times 4)$ or $c(2 \times 2)$, box 4 and box 7, respectively.

Other Coexisting Structures in Transition Metal Oxides. The coexistence of surface phases observed on oxides to date reside in two categories. In the case of $SrTiO_3(110)$, ZnO(0001), and Fe_2O_3 (0001), reconstructed terraces are attributed to the polar character of the surface. The surface neutrality and charge balance is accomplished through the termination at an anion or cation atomic layer with terraces constituting long-range defect patterns (adatoms or vacancies)[6,21] or in a periodic surface phase containing a large number of coordinated vacancies forming novel surface structures.[16,18] Enterkin *et al.*[22] presented STM and DFT data on the $SrTiO_3(110)$ surface where a (3 × 1) reconstruction contains an intergrowth of the (4 × 1) phase. The thermodynamic stability of both surfaces was ascribed to TiO_4 surface tetrahedral complexes, but the kinetics of the phases was not explored. In all these polar systems where coexistence of phases has been found, the ability to accommodate charge imbalance to restore chemical stability is presumably the main driving force. STM of $Fe_3O_4(001)$ thin films indicated the presence of coexisting domains due to stacking faults,[17] and the coexistence of a stable and a metastable surface with the presence of Fe dimers.[29,30] The domain growth of the dimer structure is not understood at present.

The case of nonpolar $SrTiO_3(001)$ is structurally similar to $BaTiO_3(001)$. Coexisting domains[8,20] and nanostructures[7,12,31] in $SrTiO_3$ have been observed using STM. Studies indicate the presence of a TiO_x
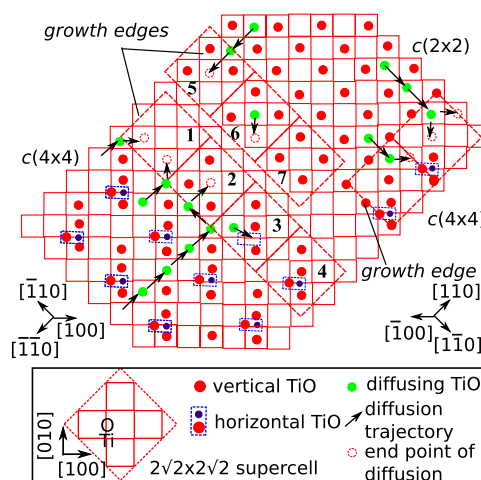

Figure 7. Domain growth and interface formation. Schematic diagram for how domains of each reconstruction can grow, eventually leading to the interfaces shown in Figure 6. Dashed squares show precursors of $c(2 \times 2)$ and $c(4 \times 4)$ in different stages of completion.

terminated surface on top of a TiO_2 layer, and surface DFT models presented therein account for the experimental observations. The relevance of the Ti:O ratio is acknowledged by these and other $SrTiO_3$ studies[6,32] as a factor in determining the surface reconstruction.

In none of these studies is the relative role of thermodynamic and kinetic factors quantified, nor is the relation of the atomic structure of the reconstruction and the interfaces between them determined, nor are the transition mechanisms contemplated. Our results accomplish this with two reconstructions not previously observed on $BaTiO_3$ and on a nonpolar surface such that the principles might be generalized to a wider range of oxide materials.

CONCLUSION

Our thermodynamic and kinetic calculations suggest that both $c(2 \times 2)$ and $c(4 \times 4)$ will likely coexist as shown in the experimental STM. Prolonged heating or higher temperatures will favor the $c(4 \times 4)$ surface, as illustrated in previous studies.[24] The coexistence of the $c(2 \times 2)$ and $c(4 \times 4)$ phases is in essence different from the cases mentioned for other transition metal oxides due to the diffusion of a TiO unit. The coexistence of these two surface reconstructions and the atomic scale structural analysis yield two important implications. First, these results demonstrate that it is possible to produce surfaces with a combination of thermodynamically stable and kinetically trapped structures which, along with the connecting interfaces, possess different and known atomic structures. Because the structures have inherently different chemical properties, this points to a strategy to engineer surface reactivity. For example, the difference in the structures between the two phases gives rise to different chemical properties of the two reconstructions, *i.e.*, differences in the

accessibility of the Ti and O adatoms toward nucleophilic and electrophilic attack, respectively, between the vertically oriented TiO and the Ti_3O_3 cluster. Second, the interface between a thermodynamically stable and a kinetically trapped metastable surface is a transitional state between two phases. These results provide an atomistic mechanism of the phase transition between the $c(2 \times 2)$ and $c(4 \times 4)$ reconstructions.

METHODS

$BaTiO_3$ single crystals are (001) oriented and one side polished. The UHV system (Omicron VT-AFM-STM) operates at a pressure of 2×10^{-10} Torr, and at room temperature. The single crystal is radiatively heated in UHV, effectively reducing it.[33] After sputtering at 600 V and 0.5 μA for 15 min[25] and two UHV annealing steps at 1100 K, we obtain the desired reconstruction. STS measurements are performed by measuring $I-V$ curves from -2 to 3 V, with feedback loop turned off. To obtain surface-LDOS from $I-V$ curves, we follow the procedure outlined by Feenstra.[34]

The surfaces were simulated using slabs with six or seven atomic layers with the in-plane supercell periodicity fixed at $0.4 \times \sqrt{2}$ nm for $c(2 \times 2)$ and $2 \times \sqrt{2}$ nm for $c(4 \times 4)$, where 0.40 nm is the $BaTiO_3$ experimental lattice constant (relaxed bulk lattice constant is 0.405 nm, $\approx$1% compressive strain is introduced). Spin-polarized DFT calculations using a planewave basis set are performed using the Quantum ESPRESSO (QE)[35] package. Calculations are done using a planewave cutoff of 50 Ry. Exchange and correlation interactions were described using the Perdew–Burke–Ernzerhof (PBE)[36] form of the generalized gradient approximation (GGA) plus Hubbard-like effective U correction to the Ti 3d states[37] (U = 4.9 eV[26]), unless otherwise stated. The core electronic states of the elements were described using norm-conserving pseudopotentials,[38–40] generated using the OPIUM code,[41] and tested previously.[42] We relaxed the atomic positions until the forces are less than 0.03 eV/Å in all directions for the atoms in the top three or four atomic layers, while we fix the bottom three layers to a bulk cubic nonpolar structure. We used $\approx$20 Å of vacuum in the direction perpendicular to the surface of the slab to prevent artificial interactions between images. The climbing image nudged elastic band method[43] was employed to calculate reaction barriers using GGA. See section I in the Supporting Information for additional theoretical details.

Conflict of Interest: The authors declare no competing financial interest.

Supporting Information Available: Additional structures explored and their corresponding simulated STM and LDOS. Structures' cif files (in zip file). Details on the mechanism of the diffusion dynamics. This material is available free of charge *via* the Internet at http://pubs.acs.org.

REFERENCES AND NOTES

1. Li, D.; Zhao, M. H.; Garra, J.; Kolpak, A. M.; Rappe, A. M.; Bonnell, D. A.; Vohs, J. M. Direct *in Situ* Determination of the Polarization Dependence of Physisorption on Ferroelectric Surfaces. *Nat. Mater.* **2008**, *7*, 473–477.
2. Wang, R. V.; Fong, D. D.; Jiang, F.; Highland, M. J.; Fuoss, P. H.; Thompson, C.; Kolpak, A. M.; Eastman, J. A.; Streiffer, S. K.; Rappe, A. M.; *et al.* Reversible Chemical Switching of a Ferroelectric Film. *Phys. Rev. Lett.* **2009**, *102*, 047601.
3. Highland, M. J.; Fister, T. T.; Fong, D. D.; Fuoss, P. H.; Thompson, C.; Eastman, J. A.; Streiffer, S. K.; Stephenson, G. B. Equilibrium Polarization of Ultrathin $PbTiO_3$ with Surface Compensation Controlled by Oxygen Partial Pressure. *Phys. Rev. Lett.* **2011**, *107*, 187602.
4. Spanier, J. E.; Kolpak, A. M.; Urban, J. J.; Grinberg, I.; Ouyang, L.; Yun, W. S.; Rappe, A. M.; Park, H. Ferroelectric Phase Transition in Individual Single-Crystalline $BaTiO_3$ Nanowires. *Nano Lett.* **2006**, *6*, 735–739.
5. Liang, Y.; Bonnell, D. A. Atomic Structures of Reduced $SrTiO_3(001)$ Surfaces. *Surf. Sci.* **1993**, *285*, L510–L516.
6. Wang, Z.; Wu, K.; Guo, Q.; Guo, J. Tuning the Termination of the $SrTiO_3(110)$ Surface by Ar^+ Sputtering. *Appl. Phys. Lett.* **2009**, *95*, 021912.
7. Castell, M. R. Nanostructures on the $SrTiO_3(001)$ Surface Studied by STM. *Surf. Sci.* **2002**, *516*, 33–42.
8. Silly, F.; Newell, D. T.; Castell, M. R. $SrTiO_3(001)$ Reconstructions: the (2×2) to $c(4 \times 4)$ Transition. *Surf. Sci.* **2006**, *600*, 219–223.
9. Becerra-Toledo, A.; Castell, M.; Marks, L. Water Adsorption on $SrTiO_3(001)$: I. Experimental and Simulated STM. *Surf. Sci.* **2012**, *606*, 762–765.
10. Erdman, N.; Poeppelmeier, K. R.; Asta, M.; Warschkow, O.; Ellis, D. E.; Marks, L. D. The Structure and Chemistry of the TiO_2-Rich Surface of $SrTiO_3(001)$. *Nature* **2002**, *419*, 55–58.
11. Lanier, C. H.; van de Walle, A.; Erdman, N.; Landree, E.; Warschkow, O.; Kazimirov, A.; Poeppelmeier, K. R.; Zegenhagen, J.; Asta, M.; Marks, L. D. Atomic-Scale Structure of the $SrTiO_3(001)$-$c(6 \times 2)$ Reconstruction: Experiments and First-Principles Calculations. *Phys. Rev. B* **2007**, *76*, 045421.
12. Marshall, M. S. J.; Becerra-Toledo, A. E.; Marks, L. D.; Castell, M. R. Surface and Defect Structure of Oxide Nanowires on $SrTiO_3$. *Phys. Rev. Lett.* **2011**, *107*, 086102.
13. Sun, L.; Denk, R.; Hohage, M.; Zeppenfeld, P. Scattering of Surface Electrons from CuO Stripes on Cu(110). *Surf. Sci.* **2008**, *602*, L1–L4.
14. Park, J. B.; Graciani, J.; Evans, J.; Stacchiola, D.; Ma, S.; Liu, P.; Nambu, A.; Sanz, J. F.; Hrbek, J.; Rodriguez, J. A. High Catalytic Cctivity of $Au/CeOx/TiO_2$ (110) Controlled by the Nature of the Mixed-Metal Oxide at the Nanometer Level. *Proc. Natl. Acad. Sci. U. S. A.* **2009**, *106*, 4975–4980.
15. Zhao, Y.; Grivel, J.-C. Controlled Growth of Epitaxial CeO_2 Thin Films with Self-Organized Nanostructure by Chemical Solution Method. *CrystEngComm* **2013**, *15*, 3816.
16. Dulub, O.; Diebold, U.; Kresse, G. Novel Stabilization Mechanism on Polar Surfaces: ZnO(0001)-Zn. *Phys. Rev. Lett.* **2003**, *90*, 016102.
17. Stanka, B.; Hebenstreit, W.; Diebold, U.; Chambers, S. Surface reconstruction of $Fe_3O_4(001)$. *Surf. Sci.* **2000**, *448*, 49–63.
18. Tang, Y.; Qin, H.; Wu, K.; Guo, Q.; Guo, J. The Reduction and Oxidation of $Fe_2O_3(0001)$ Surface Investigated by Scanning Tunneling Microscopy. *Surf. Sci.* **2013**, *609*, 67–72.
19. Luttrell, T.; Li, W.-K.; Gong, X.-Q.; Batzill, M. New Directions for Atomic Steps: Step Alignment by Grazing Incident Ion Beams on $TiO_2(110)$. *Phys. Rev. Lett.* **2009**, *102*, 166103.
20. Deak, D. S.; Silly, F.; Newell, D. T.; Castell, M. R. Ordering of TiO_2-Based Nanostructures on $SrTiO_3(001)$ Surfaces. *J. Phys. Chem. B* **2006**, *110*, 9246–9251.
21. Russell, B. C.; Castell, M. R. Reconstructions on the Polar $SrTiO_3(110)$ Surface: Analysis Using STM, LEED, and AES. *Phys. Rev. B* **2008**, *77*, 245414.
22. Enterkin, J. A.; Subramanian, A. K.; Russell, B. C.; Castell, M. R.; Poeppelmeier, K. R.; Marks, L. D. A Homologous

Series of Structures on the Surface of $SrTiO_3$(100). *Nat. Mater.* **2010**, *9*, 245–248.

23. Li, D. Domain Specific Phenomena at Ferroelectric Perovskite Surfaces. Thesis, University of Pennsylvania, 2008.

24. Kolpak, A. M.; Li, D.; Shao, R.; Rappe, A. M.; Bonnell, D. A. Evolution of the Structure and Thermodynamic Stability of the $BaTiO_3$(001) Surface. *Phys. Rev. Lett.* **2008**, *101*, 036102.

25. Morales, E. H.; Bonnell, D. A. On the Relationship between Surface Reconstructions and Step Edge Stability on $BaTiO_3$(001). *Surf. Sci.* **2013**, *609*, 62–66.

26. Martirez, J. M. P.; Morales, E. H.; Saidi, W. A.; Bonnell, D. A.; Rappe, A. M. Atomic and Electronic Structure of the $BaTiO_3$(001) $\sqrt{5}\times\sqrt{5}R26.6°$ Surface Reconstruction. *Phys. Rev. Lett.* **2012**, *109*, 256802.

27. Cardona, M. Optical Properties and Band Structure of $SrTiO_3$ and $BaTiO_3$. *Phys. Rev.* **1965**, *140*, A651.

28. DiDomenico, M.; Wemple, S. H. Optical Properties of Perovskite Oxides in Their Paraelectric and Ferroelectric Phases. *Phys. Rev.* **1968**, *166*, 565.

29. Parkinson, G. S.; Novotný, Z.; Jacobson, P.; Schmid, M.; Diebold, U. A Metastable Fe(A) Termination at the Fe_3O_4(001) Surface. *Surf. Sci.* **2011**, *605*, L42–L45.

30. Spiridis, N.; Barbasz, J.; Łodziana, Z.; Korecki, J. Fe_3O_4(001) Films on Fe(001): Termination and Reconstruction of Iron-Rich Surfaces. *Phys. Rev. B* **2006**, *74*, 155423.

31. Liang, Y.; Bonnell, D. Effect of Variations in Stoichiometry on the Surface Structure of $SrTiO_3$(001). *J. Am. Ceram. Soc.* **1995**, *78*, 2633–2640.

32. Wang, Z.; Yang, F.; Zhang, Z.; Tang, Y.; Feng, J.; Wu, K.; Guo, Q.; Guo, J. Evolution of the Surface Structures on $SrTiO_3$-(110) Tuned by Ti or Sr Concentration. *Phys. Rev. B* **2011**, *83*, 155453.

33. Aberdam, D.; Bouchet, G.; Ducros, P. LEED Study of Surface Structures on the (001) Face of $BaTiO_3$. *Surf. Sci.* **1971**, *27*, 559–570.

34. Feenstra, R. M. Tunneling Spectroscopy of the (110) Surface of Direct-Gap III-V Semiconductors. *Phys. Rev. B* **1994**, *50*, 4561–4570.

35. Giannozzi, P.; Baroni, S.; Bonini, N.; Calandra, M.; Car, R.; Cavazzoni, C.; Ceresoli, D.; Chiarotti, G. L.; Cococcioni, M.; Dabo, I.; *et al.* Quantum ESPRESSO: A Modular and Open-Source Software Project for Quantum Simulations of Materials. *J. Phys.: Condens. Matter* **2009**, *21*, 395502.

36. Perdew, J. P.; Burke, K.; Ernzerhof, M. Generalized Gradient Approximation Made Simple. *Phys. Rev. Lett.* **1996**, *77*, 3865–3868.

37. Cococcioni, M.; de Gironcoli, S. Linear Response Approach to the Calculation of the Effective Interaction Parameters in the LDA $+$ U Method. *Phys. Rev. B* **2005**, *71*, 035105.

38. Rappe, A. M.; Rabe, K. M.; Kaxiras, E.; Joannopoulos, J. D. Optimized Pseudopotentials. *Phys. Rev. B Rapid Comm.* **1990**, *41*, 1227–1230.

39. Ramer, N. J.; Rappe, A. M. Designed Nonlocal Pseudopotentials for Enhanced Transferability. *Phys. Rev. B* **1999**, *59*, 12471–12478.

40. Grinberg, I.; Ramer, N. J.; Rappe, A. M. Quantitative Criteria for Transferable Pseudopotentials in Density Functional Theory. *Phys. Rev. B* **2001**, *63*, 201102(R).

41. Opium—Pseudopotential Generation Project. http://opium.sourceforge.net.

42. Al-Saidi, W. A.; Rappe, A. M. Density Functional Study of $PbTiO_3$ Nanocapacitors with Pt and Au Electrodes. *Phys. Rev. B* **2010**, *82*, 155304.

43. Henkelman, G.; Uberuaga, B. P.; Jónsson, H. A Climbing Image Nudged Elastic Band Method for Finding Saddle Points and Minimum Energy Paths. *J. Chem. Phys.* **2000**, *113*, 9901–9904.